

Acoustic Shadow Detection From Scanline Statistics of B-Mode and Radiofrequency Ultrasound Data of Different Anatomy and Transducers

Ricky Hu^{a,*}, Rohit Singla^a, Farah Deeba^a, Robert N. Rohling^a

^aDepartment of Electrical and Computer Engineering, University of British Columbia, Vancouver, Canada

Abstract

An acoustic shadow is an ultrasound artifact occurring at boundaries between significantly different materials, resulting in a continuous dark region on the image. Shadow detection is important as shadows can identify anatomical features or obscure regions of interest. A study was performed to scan human subjects (N=35) specifically to explore the statistical characteristics of shadows. Subjects were scanned using different transducers and anatomy for a general investigation of shadows as previous studies focused on shadows created by specific imaging scenarios. Shadow detection methods were then developed by analyzing the statistics of patches of radiofrequency (RF) or brightness-mode (B-mode) data if RF data is unavailable. Both methods utilized adaptive thresholding, needing only the transducer pulse width as an input parameter for easy utilization by different operators or equipment. Mean Dice coefficients (\pm standard deviation) of 0.90 ± 0.07 and 0.87 ± 0.08 were obtained for the RF and B-mode methods, which is within range of manual annotators. The results indicate that the methods are able to detect shadows with high versatility in different imaging scenarios. Shadows were analyzed by ultrasonic speckle, providing future studies with statistical characteristics to further understand shadows. The detection methods and shadow analysis can also potentially aid interpretation of ultrasound images or serve as an important pre-processing step for machine learning methods.

Keywords: Acoustic Shadow, Ultrasound, Speckle, Radiofrequency, Segmentation

1 Introduction

Ultrasound devices have become increasingly affordable and portable, encouraging applications such as point-of-care ultrasound (Bouhemad et al., 2011), novice usage (Becker et al., 2016), and creating training data sets for machine learning (Ghose et al., 2013). However, ultrasound is susceptible to unique artifacts that increase the difficulty of interpretation and processing of images. One artifact is an acoustic shadow, which occurs when an ultrasound wave propagates to a boundary of two materials with high impedance differences (Kremkau and Taylor, 1986). The wave is almost completely reflected and beyond the boundary is a continuous dark region and a loss of anatomical features. Shadows occur in air-tissue, tissue-bone, and tissue-lesion interfaces. Shadows can aid interpretation, such as identifying gall stones (Good et al., 1979) or spinal levels (Galiano et al., 2005). However, shadows, such as from poor transducer contact, can lead to misinterpretation of anatomy, particularly by novice users and automated processing algorithms. Thus, the identification of shadows is an important preprocessing step in many applications.

Several methods have been used in literature to detect shadows. Geometric techniques model the path of an ultrasound signal for an expected image along the scanline using a random walk (Karamalis et al., 2012). Pixels are then flagged as a shadow if it is below a confidence threshold. However, geometric techniques require knowledge of ultrasound transducer properties to parameterize random walk weights, such as the focal length, radius of curvature, and thickness. The technique would be cumbersome to implement across different ultrasound machines. This also reduces applicability for machine learning applications as accurate transducer parameter labels are required for each image.

Pixel intensity methods ignore the transducer properties and analyze only the graphical properties of an image (Hellier et al., 2010). Shadows have been detected on brain images by analyzing the entropy along a scanline to flag pixels of sudden low entropy as a potential shadow. The technique achieved a comparable Dice similarity coefficient as geometric methods but require specific thresholding, window sizing, filtering, and image mask parameterization for different anatomy and transducers. This method would be infeasible in a clinical setting, particularly for novice users or point-of-care applications, as parameterization requires image processing expertise.

Machine learning methods have gained significant interest in medical imaging analysis. To our knowledge, no

*Corresponding Author: Ricky Hu, Robotics and Control Laboratory, University of British Columbia, Room 3090, 2332 Main Mall, Vancouver, BC, Canada V6T 1Z4. Email: rhu@ece.ubc.ca

machine learning method has demonstrated capability of
 general shadow detection from multiple anatomy. Deep
 learning methods have identified features in a specific im-
 age sets that contains a shadow, such as neuroanatomical
 regions in cranial scan (Milletari et al., 2017) or spinal
 levels in a posterior scan (Hetherington et al., 2017). Al-
 though machine learning has the potential of providing
 automated feature recognition in multiple applications, a
 large data set is required for an algorithm to recognize cer-
 tain features. Ultrasound imaging is highly variable due
 to unique artifacts, operator technique, and equipment. In
 addition, shadows are a very general feature that occur in
 various imaging scenarios. Previous techniques focus on
 a single anatomical region and training data was from a
 consistent imaging scenario. However, it is difficult to con-
 struct a training data set with the generality required to
 recognize shadows in different scenarios usable for a variety
 of ultrasound applications.

There are two objectives to the study. First, to address
 the need of understanding general characteristics of shad-
 ows, a study was conducted to scan multiple anatomy and
 transducers specifically to analyze the statistics of differ-
 ent types of shadows. Second, to address existing needs for
 versatile detection and limiting parameterization, previous
 methods were then extended utilizing statistical threshold-
 ing of radiofrequency (RF) or brightness-mode (B-mode)
 data to detect the full range of shadows.

Materials and Methods

Data Collection

Ultrasound RF and B-mode data was acquired by scan-
 ning 37 adult participants with informed written consent,
 approved by the University of British Columbia Research
 Ethics Board (Study ID: H18-01199). The scans included a
 forearm scan near the distal end of the pronator quadratus,
 an elbow scan near the cubital fossa, and a rib scan on the
 anterior surface of right ribs 11-12. Each scan was taken
 with both a curvilinear (C5-2/60, Ultrasonix, Canada) and
 linear (L14-5/38, Ultrasonix, Canada) transducer. Differ-
 ent transducer settings were used for each anatomical re-
 gion and transducer, summarized in Table 1. Shadows are
 expected to occur due to bones in the arm and from an air
 gap created by the lateral edges of the curvilinear trans-
 ducer not being in flush contact with the skin. The ex-
 periment was designed to generate a dataset from various
 imaging scenarios to explore general shadow characteris-
 tics and to validate the versatility of the shadow detection
 methods.

Radiofrequency Speckle Analysis

To analyze shadows, patches of speckle was analyzed
 on the RF signal. Speckle occurs due to multiplicative
 scattering of acoustic waves in a material, resulting in a
 granular patch on the image. The benefit of RF analy-
 sis is that B-mode image processing commonly attempts

to remove speckle, but speckle contains information of the
 acoustic interactions in tissue (Burckhardt, 1978). Speckle
 can then characterize different regions, such as a region of
 tissue or a region of signal loss in a shadow. In addition,
 B-mode data can be manipulated by an operator to visu-
 ally enhance an image, such as adjusting time-gain com-
 pensation or dynamic range. Thus, speckle analysis can
 provide shadow detection usable across different machines
 and operators.

One of the first models for speckle is with a one param-
 eter Rayleigh distribution to model the probability density
 of a random walk (Burckhardt, 1978). The Rayleigh dis-
 tribution is capable for modeling fully developed speckle,
 which does not occur in limited scattering (Tuthill et al.,
 1988). More generalized models have been applied such as
 the Rician, Homodyned-K, and Nakagami distributions to
 characterize speckle (Destremes and Cloutier, 2010). The
 utility of speckle has been demonstrated in literature to
 classify tumorigenicity of breast lesions (Byra et al., 2016)
 or levels of liver fibrosis (Ho et al., 2012) by categorizing
 image regions based on the speckle pattern. Shadow char-
 acterization presents a simpler problem as a shadow and
 non-shadow region contain significantly different speckle
 patterns. Thus, the Nakagami distribution expressed in
 Eq. 1 was chosen to model speckle. The Nakagami distri-
 bution provides greater generality than the Rayleigh distri-
 bution while being more computationally efficient than the
 Rician or Homodyned K distributions (Destremes and
 Cloutier, 2010).

$$\Phi(x, \mu, \omega) = 2\left(\frac{\mu}{\omega}\right)^{\mu} \frac{1}{\Gamma(\mu)} x^{(2\mu-1)} e^{-\frac{\mu}{\omega} x^2} \quad (1)$$

Where x is the RF intensity, μ is the shape parameter,
 ω is the scale parameter and $\Gamma(\mu)$ is the gamma distribu-
 tion.

To characterize shadows, the raw RF data was first
 processed by computing the echo envelope of each scan-
 line with a Hilbert transform. An absolute logarithmic
 scale of the echo envelope was taken to generate an “RF
 Image”, visually similar to B-mode but without filtering to
 remove speckle. Next, the RF image was divided into over-
 lapped patches with a width of a single RF data point and
 a length of three times the pulse width. This patch size
 was demonstrated in literature to be sufficiently large to
 capture multiple wavelengths and scattering events while
 being small enough to be useful in differentiating different
 regions on the millimeter scale (Byra et al., 2016). Next,
 the RF data in each patch was fit to a Nakagami distribu-
 tion using a maximum likelihood estimate to compute the
 fitted Nakagami shape and scale parameters μ and ω , pro-
 ducing a map of Nakagami parameter values for an image
 as shown in Fig. 1.

To detect shadows, a simple automated thresholding
 scheme was used. Otsu’s method was applied on the en-
 tire image to compute a threshold for the Nakagami ω
 parameter. This was sufficient as the Nakagami ω pa-
 rameter is significantly different for shadow regions with

abundant speckle and non-shadow regions with minimal speckle. Then, for each scanline, the deepest data point that is above the threshold is labeled as the shadow boundary and all data points below are labeled as a shadow.

B-mode Scanline Analysis

Many ultrasound machines do not provide access to RF data for speckle analysis. Thus, a previous pixel-intensity shadow detection method on B-mode images was modified and extended. Scanline entropy was investigated on B-mode images to characterize different types of shadows. Adaptive thresholding of entropy was then applied for shadow detection to address the need for usability across different equipment with minimum configuration. First, the cumulative scanline entropy is computed for each pixel, similar to the ‘‘Rupture Criterion’’ (Hellier et al., 2010), with the window size fixed as three times the pulse width, η , as defined in Eq. 2

$$S_{i,j} = \sum_{i=1}^{3\eta} I(i-1) \log_2 \frac{I(i-1)}{I(i+1)} + I(i+1) \log_2 \frac{I(i+1)}{I(i-1)} \quad (2)$$

Where $S_{i,j}$ is the cumulative entropy at pixel i on scanline j , η is the pulse width, $I(i)$ is the pixel intensity of i .

For linear images, tracking scanlines is simple. For curvilinear images, the scanline paths were tracked by capturing the slope of the lateral edges by following the ring-down regions. Ring-down is a consistent artifact that produces bright bands at the top of an image due to the fluid in the transducer reflecting a continuous signal. The scanlines were then interpolated between the slopes of the lateral edges.

Next, Otsu’s method is applied similarly to compute a threshold entropy value. The intuition of the threshold is different than in RF analysis. In RF analysis, the threshold separates patches of intense and minimal speckle. In B-mode analysis, the threshold separates pixels of a shadow boundary, which has high entropy, and pixels not of a shadow boundary, which include shadow and non-shadow regions. Thus, shadows can be identified by finding the last pixel on a scanline with an entropy higher than the threshold, representing a bright shadow boundary.

Validation

A trained annotator manually outlined shadow regions on B-mode images. The manual regions were used as a gold standard, as manual identification is common in clinical practice and has been used in previous literature for comparison (Hellier et al., 2010). A Dice coefficient was computed to compare similarity of manual and automated shadow detection.

Results

Examples of detected shadows from both methods are highlighted in gray in Fig. 2 in different imaging scenarios. The Dice coefficients for both methods for different anatomy and transducers are shown in Table 2. The mean Dice coefficients (\pm standard deviation) were 0.90 ± 0.07 and 0.87 ± 0.08 for RF and B-mode methods. Manual annotation was repeated five times with a mean Dice coefficient of 0.92 ± 0.02 for all images and transducers.

With the benefit of a varied dataset, general characteristics of shadows can be analyzed. The log-scale Nakagami ω parameter recorded a mean \pm standard deviation of 13.95 ± 2.03 for all non-shadow and 8.89 ± 1.16 for shadow regions defined by manual outlining of all images. The μ parameter recorded 1.02 ± 0.29 for non-shadow and 3.25 ± 2.35 for shadow-regions.

Discussion

The RF and B-mode shadow detection developed achieved a high Dice similarity coefficient for all anatomy and transducer types. Previous studies reported that the Dice coefficient between manual annotators recorded a mean of 0.91 ± 0.07 (Hellier et al., 2010). Every scenario detected from both methods achieved a Dice coefficient within the range of manual detection within operator variability. An important feature of shadow detection is being able to differentiate between a shadow and attenuation of the signal. Both scenarios result in an eventual loss of signal. Shadow detection, however, has a characteristic high intensity shadow boundary before a significant loss in signal, compared to gradually signal losses in attenuation. Both methods were capable of this distinction. The high accuracy supports the versatility of the detection method as both methods are able to identify shadows across different anatomy and transducers with minimum configuration.

In RF detection, both false positive and false negative errors most frequently occurred immediately below a shadow boundary as opposed to B-mode detection where errors were in various regions. The Nakagami distributions in patches near the boundary resemble distributions for non-shadows. Moreover, granular RF speckle can be visually observed in a neighborhood around a boundary. The speckle gradually lessens after a brightest point on a scanline, possibly due to incomplete total reflection at a boundary. This indicates that the boundary is not an instantaneous division between non-shadow and shadow, rather, there is a ‘‘transition region’’ before the image fully resembles a shadow with a loss of signal. In previous literature, shadows were defined qualitatively (Kremkau and Taylor, 1986) as a sudden loss of signal and brightness. The observed transition region in this study suggests that the qualitative definition of a shadow may be insufficient for accurate detection. One algorithm may detect the shadow starting immediately after the brightest location, or another may use a convention such as a full width at

half maximum to define where the signal has sufficiently low intensity to resemble the start of a shadow. There is a need for a clear definition for where a shadow begins to improve shadow detection accuracy, both from a signaling perspective for image processing and a visual perspective for manual inspection.

For a general observation for shadows, the computed Nakagami ω parameter of all manually outlined shadows indicate that there is a statistically significant difference between shadow and non-shadow regions, even with the error in the transition regions considered. The speckle from shadows is thus distinct from the speckle created by tissue, muscle, or fat. This is likely due to shadows representing a region where almost no acoustic speckle interactions occur as the waves have been reflected at a preceding boundary.

The findings in this study result in several implications. First, the statistics of acoustic shadows have been investigated on a dataset with shadows occurring from multiple scenarios as opposed to specific cases where shadows are observed. This provided a more generalizable observation that shadows can be characterized by speckle distributions and that there exists a transition region before the loss of speckle in a shadow. Second, the shadow detection methods demonstrated high accuracy, indicating that accurate shadow detection is possible regardless of transducer or imaging location. In future studies, the speckle statistics observed can be used to develop further models for anatomical features containing shadows, such as training a machine learning algorithm to measure the size of gall stones. Future studies would also have to take into consideration the most frequent source of error of shadow detection as the shadow boundary. For instance, a convention can be developed for one algorithm to detect the surface of the gallstone as the brightest point on a scanline to be comparable with other images.

Conclusions

Acoustic shadows from different imaging scenarios were investigated. RF and B-mode methods were developed for acoustic shadow detection requiring only the transducer pulse width as the input parameter. When comparing to manual detection, the methods achieved a Dice similarity coefficient within range of manual observers. The work focused on applying shadow detection and statistical analysis to a varied dataset of three different anatomical locations and two different transducer to provide a representative understanding of general acoustic shadows. The statistics of acoustic shadow indicate that shadows contain a distinct speckle distribution compared to non-shadows and the speckle characteristics transition at the shadow boundary. The statistical findings of shadows can aid interpretation of ultrasound images in the future using speckle analysis. The versatility of the shadow detection method has potential to improve the interpretation of ultrasound images with shadow artifacts or to serve as a pre-processing step for machine learning methods.

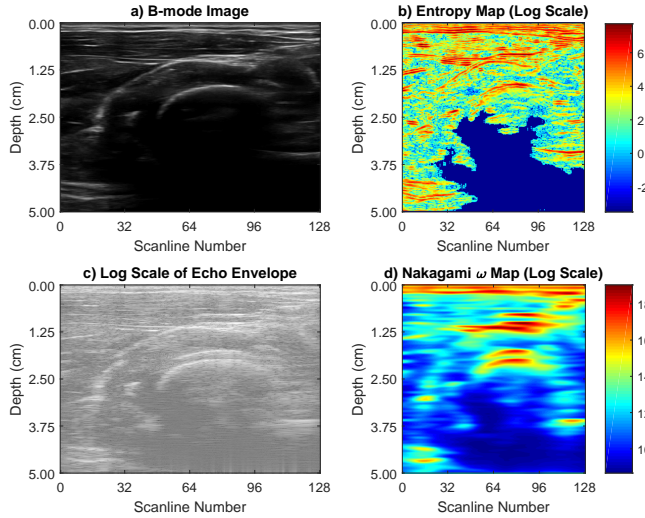
References

- Becker DM, Tafoya CA, Becker SL, Kruger GH, Tafoya MJ, Becker TK. The use of portable ultrasound devices in low- and middle-income countries: a systematic review of the literature. *Tropical Medicine & International Health*, 2016;21:294–311.
- Bouhemad B, Brisson H, Le-Guen M, Arbelot C, Lu Q, Rouby JJ. Bedside ultrasound assessment of positive end-expiratory pressure-induced lung recruitment. *American Journal of Respiratory and Critical Care Medicine*, 2011;183:341–347.
- Burckhardt CB. Speckle in ultrasound B-mode scans, 1978.
- Byra M, Nowicki A, Wróblewska-Piotrkowska H, Dobruch-Sobczak K. Classification of breast lesions using segmented quantitative ultrasound maps of homodyned K distribution parameters. *Med. Phys.*, 2016;43:5561–5569.
- Destremes F, Cloutier G. A critical review and uniformized representation of statistical distributions modeling the ultrasound echo envelope. *Ultrasound Med. Biol.*, 2010;36:1037–1051.
- Galiano K, Obwegeser AA, Bodner G, Freund M, Maurer H, Kamelger FS, Schatzer R, Ploner F. Ultrasound guidance for facet joint injections in the lumbar spine: A computed tomography-controlled feasibility study. *Anesthesia and Analgesia*, 2005;101:579–583.
- Ghose S, Oliver A, Mitra J, Martí R, Lladó X, Freixenet J, Sidibé D, Vilanova JC, Comet J, Meriaudeau F. A supervised learning framework of statistical shape and probability priors for automatic prostate segmentation in ultrasound images. *Medical Image Analysis*, 2013;17:587–600.
- Good LI, Edell SL, Soloway RD, Trotman BW, Mulhern C, Arger Pa. Ultrasonic properties of gallstones. Effect of stone size and composition. *Gastroenterology*, 1979;77:258–263.
- Hellier P, Coupé P, Morandi X, Collins DL. An automatic geometrical and statistical method to detect acoustic shadows in intraoperative ultrasound brain images. *Medical Image Analysis*, 2010;14:195–204.
- Hetherington J, Lessoway V, Gunka V, Abolmaesumi P, Rohling R. SLIDE: automatic spine level identification system using a deep convolutional neural network. *International Journal of Computer Assisted Radiology and Surgery*, 2017;12:1189–1198.
- Ho MC, Lin JJ, Shu YC, Chen CN, Chang KJ, Chang CC, Tsui PH. Using ultrasound Nakagami imaging to assess liver fibrosis in rats. *Ultrasonics*, 2012;52:215–222.
- Karamalis A, Wein W, Klein T, Navab N. Ultrasound confidence maps using random walks. *Medical Image Analysis*, 2012;16:1101–1112.
- Kremkau FW, Taylor KJ. Artifacts in ultrasound imaging. *Journal of Ultrasound in Medicine*, 1986;5:227–237.
- Milletari F, Ahmadi SA, Kroll C, Plate A, Rozanski V, Maiostre J, Levin J, Dietrich O, Ertl-Wagner B, Bötzel K, Navab N. Hough-CNN: Deep learning for segmentation of deep brain regions in MRI and ultrasound. *Computer Vision and Image Understanding*, 2017;164:92–102.
- Tuthill TA, Sperry RH, Parker KJ. Deviations from rayleigh statistics in ultrasonic speckle. *Ultrasonic Imaging*, 1988;10:81–89.

Figure Captions

Figure 1: A visualization of the B-mode and RF parameter maps. The b) Entropy Map was computed from processing of the a) original B-mode image and the d) Nakagami ω map was computed from the c) echo envelope. Note that the echo envelope contains noticeable speckle, which has been used to fit a Nakagami distribution to characterize shadow. The region at depth 2.50cm and scanlines 32-40 is attenuation and not a shadow. This is an important distinction in shadow detection and both maps show the region as below a threshold to flag a shadow boundary.

Figure 2: A comparison of the original B-mode images, the detected shadows manual detection, RF detection, and B-mode detection. Both detection methods perform similar to manual detection. Both methods perform slightly less accurately on curvilinear images, likely due to the reduced resolution from interpolating the scanlines. Most errors of RF detection occur near the shadow boundary, likely due to the transitioning speckle from non-shadow to shadow.



Tables

Table 1: Transducer properties for different imaging scenarios.

	Anatomy	Frequency	Depth	Gain
Linear Transducer (L14-5/38)	Forearm	11.0MHz	5.0cm	50%
	Elbow	11.0MHz	5.0cm	40%
	Ribcage	5.0MHz	10.0cm	30%
Curvilinear Transducer (C5-2/60)	Forearm	4.0MHz	5.0cm	50%
	Elbow	4.0MHz	5.0cm	40%
	Ribcage	3.3MHz	10.0cm	30%

Table 2: Mean Dice coefficients for different imaging scenarios \pm standard deviation.

		RF	B-Mode
Linear (L14-5/38)	Forearm	0.91 ± 0.05	0.89 ± 0.06
	Elbow	0.94 ± 0.06	0.90 ± 0.07
	Ribcage	0.87 ± 0.09	0.84 ± 0.06
Curvilinear (C5-2/60)	Forearm	0.89 ± 0.05	0.86 ± 0.08
	Elbow	0.93 ± 0.04	0.90 ± 0.09
	Ribcage	0.83 ± 0.08	0.83 ± 0.10
Mean	All Anatomy	0.90 ± 0.07	0.87 ± 0.08

